Chemical Engineering Journal 420 (2021) 130451

Contents lists available at ScienceDirect

Chemical Engineering Journal

journal homepage: www.elsevier.com/locate/cej

A synergetic SnSb-amorphous carbon composites prepared from polyesterification process as an ultrastable potassium-ion battery anode

Yi-Yen Hsieh [1], Kuan-Ting Chen [1], Hsing-Yu Tuan [*]

Department of Chemical Engineering, National Tsing Hua University, Hsinchu 30013, Taiwan

ARTICLE INFO

Keywords:
Potassium ion battery
Synergetic effect
Anode
Full cell

ABSTRACT

Combining the stability of amorphous carbon with the high-capacity contribution of metal alloys need explicit structural engineering design so that the beneficial contribution of each constituent material can lead to the desired synergistic electrochemical performance. Here, we report the synthesis of ultrafine SnSb embedded in meso/microporous amorphous carbon (SnSb@MAC) through a polyesterification strategy. As the anode of potassium ion batteries (PIBs), SnSb@MAC composite exhibits better electrochemical performance relative to that of SnSb nanocrystals (SnSb NCs) and MAC. In particular, the composite has an excellent cycle life, with a reversible capacity of ~200 mA h g^{-1} after 5000 cycles, being the longest life reported for the SnSb-C composites. The K^+-transport mechanism of the composite is experimentally verified through *in-situ* X-ray diffraction, *ex-situ* TEM and selected area electron diffraction (SAED) and demonstrate the high synergy between SnSb and MAC resulted in the satisfactory storage performance. Finally, the full cell constructed by coupling the SnSb@MAC anode with an organic cathode (perylene-3,4,9,10-tetracarboxylic dianhydride, PTCDA) exhibits a maximum energy density of 228.9 W h kg^{-1} and a maximum power output of 6150 W kg^{-1} as well as 177 mA h g^{-1} along with a current density of 400 mA g^{-1} after 400 cycles.

1. Introduction

Potassium-ion batteries (PIBs) have achieved intense attention, and it is estimated that can deliver sufficient energy densities and lower cost due to their higher operation voltage and the abundance of potassium source in the earth's crust and can be widely used in grid-scale energy storage. Focusing on the advantage of electrochemistry of PIBs, it has a fast K^+ transfer capability due to the smaller Stokes radius in the nonaqueous electrolyte. Nonetheless, challenges remain, and suitable materials need to be designed to accommodate the larger size of desolvated K^+. There are many strategies that can be used to control interface chemistry, reduce volume changes, adjust electronic structure, and avoid excessive side reactions, such as nano- or micro-engineering design, heteroatom doping, use of buffer matrix, and optimization of electrolytes [1,2].

Carbon-based anodes have been extensively studied due to their low price, good electrical conductivity, and structural stability during intercalation/deintercalation process. For example, Lu et al., presented a sulfur-assisted method that converts benzene rings of tetraphenyltin into high purity crystalline graphene which proved ideal for PIB applications (230 mAh g^{-1} at current density of 0.2 A g^{-1} after 1000 cycles) [3]. Yang *et al.,* design a porous 3D carbon network doped with nitrogen, sulfur and oxygen via a carbonization-etching strategy, which exhibited a capacity of 100 mA h g^{-1} at 0.5 A g^{-1} after 1000 cycles. The porous structure significantly reduces the resistance of charge transfer and improves the transmission of K^+ [4]. The nitrogen-doped carbon fiber used in the composite material shows capacities of 140 to 200 mA h g^{-1} at various current rates of 0.5 to 2.0 mA g^{-1}, meaning that the stable structure of carbon supports the rate capability [5]. Unlike crystalline graphite, amorphous ordered mesoporous carbon has a layered structure in a short range, which can accommodate more K^+ into the carbon layer, tolerates volume expansion, and perform a capacity of 150 mAh g^{-1} at 1.0 A g^{-1} after 1000 cycles [6]. However, their relatively low capacity (<200 mAh g^{-1}) cannot meet the demand for sufficient energy output, which hinders the advantages of PIB commercial applications. Most importantly, the amorphous carbon materials can deliver the higher capacity and better cyclability than that of crystalline carbons in potassium-ion system [7-11].

* Corresponding author.
E-mail address: hytuan@che.nthu.edu.tw (H.-Y. Tuan).
[1] These authors contributed equally to this work.

https://doi.org/10.1016/j.cej.2021.130451
Received 12 March 2021; Received in revised form 7 May 2021; Accepted 18 May 2021
Available online 24 May 2021

Compared with carbon-based anodes, alloying or conversion materials have a high gravimetric capacity, and can offer a high operating potential. As a PIB anode, the most common metal is antimony (Sb), and it has a high theoretical capacity of ~660 mA h g^{-1} in the three-electron alloying reaction (K_3Sb). However, mono-element materials (e.g. Sb, Sn, Bi, P) severe dramatic volume change and associated pulverization during the insertion of desolvated K^+. It's worth noting that the dualistic metal alloys can perform better capacity retention due to the synergetic effect and different reaction potential [12-18]. Despite several studies on binder composition, electrolyte optimization, and carbon scaffold design being conducted, how to achieve the ultra-long cycle life of the composite anode remains challenge [19,20]. Recently, the concept of "composite" which is defined as the mixture of carbon and metal materials has been adopted for the above-mentioned problems [20-22]. Both metal and carbon in the composite materials are important for improving and enhancing the electrochemical performance and cycling life. Xu *et al.,* synthesized the MOFs-derived ZnSe@ N-doped carbon composite by pyrolysis and selenization, which delivers a specific capacity of 132.9 mA h g^{-1} after 1200 cycles at 0.1 A g^{-1} [23]. Furthermore, Sun *et al.,* encapsulate phosphorus nanoparticles into a commercial porous carbon through the use of evaporation and condensation strategy for, with excellent cycle capacity and rate capability (212 mA h g^{-1} at 3.2 A g^{-1} over 10,000 cycle) [24]. Wang *et al.,* used the oleylamine-assisted solvothermal method to produce amorphous carbon coated on the surface of WSe_2, the conductivity of nanosheets can be improved and the carbon can buffer volume change, which is beneficial to rate performance and cycle stability (209 mAh g^{-1} at 1.0 A g^{-1} over 500 cycles) [25]. Luo *et al.,* also used MoO_2 embedded in rGO and 3D porous carbon to enhance the electrochemical performances in PIBs [26,27].

In this study, we conduct a systematic investigation on the storage performance of ultrafine SnSb embedded in meso/microporous amorphous carbon (termed as SnSb@MAC composite) through a polyesterification strategy. The synergistic effect of SnSb and amorphous carbon composite material shows electrochemical performance, with a gravimetric capacity of ~350 mA h g^{-1} at 50 mA g^{-1} and an excellent shelf life with a demonstrated capacity of ~200 mA h g^{-1} after 5000 cycles. Nano-engineering design and mesoporous carbon can improve ion or electron transfer, thereby enhancing electrochemical stability and performance. *In/ex-situ* microscopy and spectroscopy results verify the reaction mechanism of SnSb@MAC with K^+ regarding its electrochemical ultrastability. The maximum energy density of PIB full cells constructed by coupling the SnSb@MAC anode with an organic cathode of perylene-3,4,9,10-tetracarboxylic dianhydride (PTCDA) is 228.9 Wh kg^{-1}, and the maximum power density is 6150 W kg^{-1}. Compared with the other reported results of SnSb composites, the cycle capacity of half cells and the energy densities of PIB full cells have been significantly improved.

2. Experimental section

2.1. Material preparation

2.1.1. Synthesis of SnSb@MAC composites

SnSb@MAC composite was synthesized via a polyesterification method [28]. Typically, 1.0 mmol antimony triacetate (Sb $(CH_3COO)_3$) (Sigma Aldrich) and 1.0 mmol tin tetraacetate (Sn $(CH_3COO)_4$) (Sigma Aldrich) were first dissolved in 10 ml ethylene glycol (Acros Organics, 99+%) and ultrasonicated for 30 min. Afterwards, 4 mmol citric acid (Sigma Aldrich, anhydrous) was added into above solution that was then stirred for 1 h to achieve homogeneous solution. Subsequently, the solution was heated at 170 °C until the product become a brown gel. After annealing the gel at 600 °C for 2 h in a tube furnace under H_2/Ar (33%) flow with a heating rate of 3.5 °C min^{-1}, the black powder was milled and collected. Besides, the MAC, Sn@C and Sb@C were obtained by same method.

3. Synthesis of SnSb nanocrystals

SnSb NCs were prepared through colloidal synthesis [29]. First, a solution of 32 mmol $NaBH_4$ (Sigma Aldrich, 99%) dissolved in 17 ml anhydrous 1-methyl-2-pyrrolidone (NMP, Sigma Aldrich, 99.5%) is heated to 60 °C under argon atmosphere. Upon reaching 60 °C, the solution of 1 mmol $SnCl_2$ (Sigma Aldrich, 98%) in 1.5 ml NMP was injected, followed by the injection of 1 mmol $SbCl_3$ (Alfa Aesar, 99+ %) and immediately cooling down to room temperature by a water–ice bath. The powder was centrifugated and washed with DI-water to remove side products. After drying at room temperature, the black product was stored in glove box.

4. Preparation of PTCDA

The perylene-3,4,9,10-tetracarboxylic dianhydride (PTCDA, Sigma Aldrich) was prepared by annealing at 450 °C for 4 h under argon flow with a heating rate of 5 °C min^{-1} [30]. The crimson powder was stored in glove box with argon atmosphere.

5. Material characterization

The morphologies of the obtained samples were investigated using scanning electron microscopy (SEM, Hitachi SU8010) equipped with energy-dispersive X-ray spectroscopy (EDS) detector. Transmission electron microscopy (TEM) (JEOL, JEM-ARM200FTH, serviced provided by NTHU and NCTU) with an accelerating voltage of 200 kV for investigating structural analysis including morphology, crystal d-spacing, and selected-area electron diffraction (SAED). The structural evolution and composition were identified using X-ray diffraction (Bruker, D8 ADVANCE) with Cu-Kα radiation (λ = 1.54 Å) and the oxidation states of the samples were characterized by high-resolution X-ray photoelectron spectrometer (XPS, ULVAC-PH, PHI QuanteraII). All the spectra obtained from XPS analysis were first calibrated by referencing the standard binding energy of C 1 s (284.8 eV), followed by the curve fitting using the software of XPSPEAK VER. 4.1. Carbon content (wt%) was carried out using NCHS (elementar vario EL cube and thermo Flash 2000, NTU). The BET surface area and BHJ pore distribution were conducted by Micromeritics ASAP 2060 in NIRI.

6. Electrochemical characterization

Utilizing a microbalance with 0.1 μg resolution (Sartorius SE2), accurate weight of active materials was measured for calculating specific capacity. The weight ratio of anode and cathode was based on 6:2:2 (SnSb@MAC: super P: NaCMC) and 8:1:1 (PTCDA: super P: NaCMC). The slurry was uniformly spread on Cu foil (or Al foil) and dried at 80 °C for 1 h under vacuum oven. Typical mass loading on SnSb@MAC and PTCDA were 0.8 ~ 0.9 mg cm^{-2} and 1.3 mg cm^{-2}, respectively. For electrochemical test, the half cells were assembled with the potassium foils as the counter electrode, a solution of 4 M Potassium bis(fluorosulfonyl)imide (KFSI, Chemical Block, 97%) in 1,2- dimethoxyethane (DME, anhydrous 99.5%) as electrolyte,[31] and Glass fiber filters (Advantec.) as a separator. All above were evenly stacked for assembling the coin cells (CR2032) in the glovebox. All electrochemical analysis of anode and cathode electrodes were carried out by employing Maccor Series 4000 and VMP3 instruments. The voltage range of electrochemical test for SnSb@MAC composites and PTCDA electrodes are 0.01–2.2 V (vs. K/K^+) and 1.5–3.5 V (vs. K/K^+), respectively.

7. Coin full cell of SnSb@MAC//PTCDA

For the CR2032 full cell, the mass ratio of SnSb@MAC to PTCDA was ~0.5 which is calculated based on the areal capacity (mA h cm^{-2}) at current density of 500 mA g^{-1}. Furthermore, both SnSb@MAC anode and PTCDA cathode were pre-potassiated for three cycles under 500 mA

g^{-1} with 4 M KFSI in DME before assembly. The potential window of electrochemical test for full cell was ranged from 0.5 V to 3.4 V.

8. Operando XRD techniques

The operando XRD patterns of SnSb@MAC were achieved from Bruker D8 ADVANCE diffractometer for first three cycles. The investigated slurry coated on Al foil as the working electrode (mass loading of active materials: ~1.0 mg), potassium metal foil as the counter and reference electrode, and 4 M KFSI in DME as the electrolyte. A current rate of 50 mA g^{-1} was settled for cycling process between 0.01 and 2.2 V (E_w vs K^+/K).

9. Results and discussion

SnSb@MAC composite are synthesized via a facile polymeric precursor route [32], also termed as the sol–gel method, as shown in Fig. 1. Initially, citric acid and metal cations form polychelates in homogeneous solution, afterwards, these complexes undergo polymerization and cross-linked reaction with ethylene glycol at 170 °C to form a polymeric resin. In addition, the cross-linking polymer structure can improve the stability of Sn-(citrate) and Sb-(citrate) embedded in the resin. In the process of calcination and pyrolysis process under H_2/Ar atmosphere, the uniformly distributed polycationic Sn and Sb undergo thermal reduction reaction to produce metal Sn and Sb, and then alloyed at the same time [33]. Finally, a composite material with ultrafine SnSb firmly embedded in MAC is obtained.

The representative results of SnSb@MAC composite obtained by polyesterification used to form SnSb nanoparticles are shown in Fig. 2. The XRD pattern of the SnSb@MAC can be indexed to a Rhombohedral crystal phase with R3m 3^- m (166) space group. The peak position of the SnSb@MAC composite is the same as the peak corresponding to the SnSb alloy in the database (PDF#33–0118, Fig. 2**a**). The diffraction pattern of MAC pyrolyzed from organic substances is presented in **Fig. S1**. During the pyrolysis process, polymerization and cross-linking reactions occur, and then the non-carbon elements appear and transform into volatile substance combined with carbon or other elements. Although some Sn peaks other than the indexed SnSb peaks are observed, the intensity of Sn is relatively low compared to the (101) plane of SnSb. The FESEM image of the SnSb@MAC composite is shown in **Fig. S2**. Nonetheless, the ultrasmall SnSb covered by thick carbon cannot be clearly seen using a SEM instrument. Hence, the TEM images in Fig. 2**b** reveal the SnSb@MAC composite, in which high-density dispersed SnSb nanoparticles are embedded in MAC. The ring pattern of the SnSb@MAC (Fig. 2**c**) consists of six diffraction rings corresponding to (101), (110), (021), (202), (211) and (122) crystal planes, respectively. The size distribution of the SnSb (average diameter: ~6 nm) is given (Fig. 2**d and 2e**). Fig. 2**f** reveals a high-resolution TEM image with interplanar d-spacings of 3.06 Å corresponding to the (101) phase of SnSb. In addition, the carbon content of SnSb@MAC is about 47 wt% according to the results obtained from element analysis of the NCHS instrument. The EDS mapping further proved the well-distributed Sn and Sb signals in this composite (Fig. 2**g**), which is consistent with a material with a composition close to SnSb with a slightly higher Sn ratio. Compared with SnSb@MAC, SnSb NCs, Sb@C and Sn@C prepared via colloidal synthesis and polyesterification strategy, respectively, showed the diameters of SnSb NCs, Sn@C and Sb@C of ~30 nm (**Fig. S3**), 20 nm (**Fig. S4**) and 110 nm (**Fig. S5**), sequentially. Therefore, the ultrasmall size of SnSb embedded in MAC can ascribe to the effect of critic acid and Sn-based alloy.

In order to deeply understand the relationship between SnSb and carbon prepared by polyesterification method, the XPS analysis of Sb 3d peaks (Fig. 3**a**) and Sn 3d peaks (Fig. 3b) can be fitted into Sb $3d_{3/2}$ (540.7 eV), Sb $3d_{5/2}$ (531.5 eV), Sn $3d_{3/2}$ (496.1 eV), and Sn $3d_{5/2}$ (487.6 eV). The binding energy of Sb $3d_{5/2}$ is higher than that of Sb^{3+} (529.8 eV) and Sb^0 (528.6 eV), being attributed to the presence of antimony oxide ($Sb_{x1}O_{y1}$). Similarly, the binding energy of Sn $3d_{5/2}$ at 487.6 eV is also higher than that of Sn^0 (485.0 eV) and Sn^{2+} (487.0 eV) and lower than that of Sn^{4+} (497.3 eV), indicating metal oxide ($Sn_{x2}O_{y2}$) on the surface of the alloy. However, both $Sn_{x2}O_{y2}$ and $Sb_{x1}O_{y1}$ are probably amorphous since there is no characteristic XRD signal associated with metal oxides, suggesting that a small amount of amorphous oxides was formed [34]. Amorphous metal oxides can be produced by the pyrolysis of metal-citrate complexes surrounding the surface of the alloy during annealing [35] or air-oxidation [36]. Besides, the fitted C = C bond in Fig. 3c reveals that the chelation of metal ions with polymeric acid can improve the dispersion of metals in the carbon precursor unit, leading to better catalytic graphitization effect. According to the Raman result given in Fig. 3d, there are different effects of SnSb disorder and sp^2 vibration structure with/without SnSb. The intensity ratio of the D-band and the G-band of the MAC embedded with SnSb is smaller than that of the MAC without catalytic SnSb, which slightly increases the vibration characteristics of the in-plane sp^2 [37]. This result shows that under the synergetic effect of metal and carbon, the graphitization property is

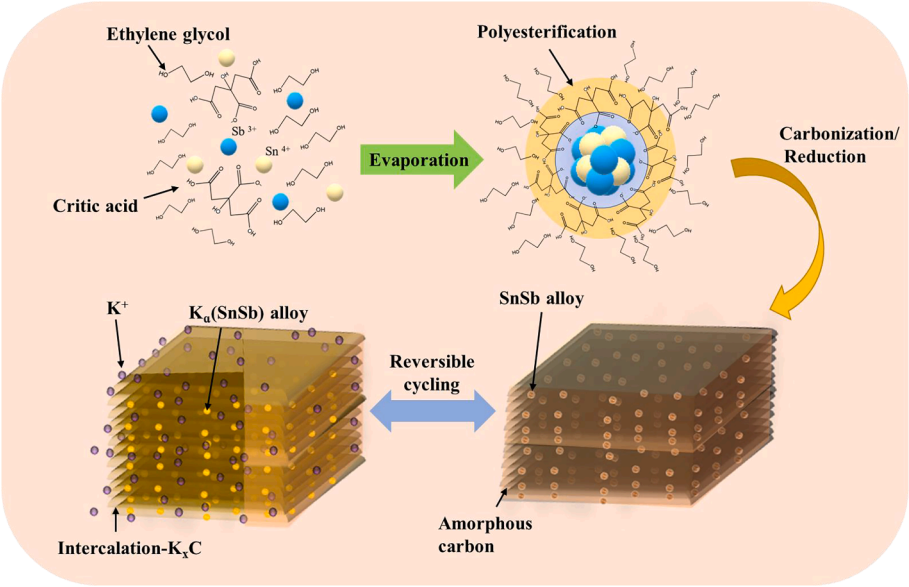

Fig. 1. Schematic illustration of SnSb@C synthesis and reversible cycling.

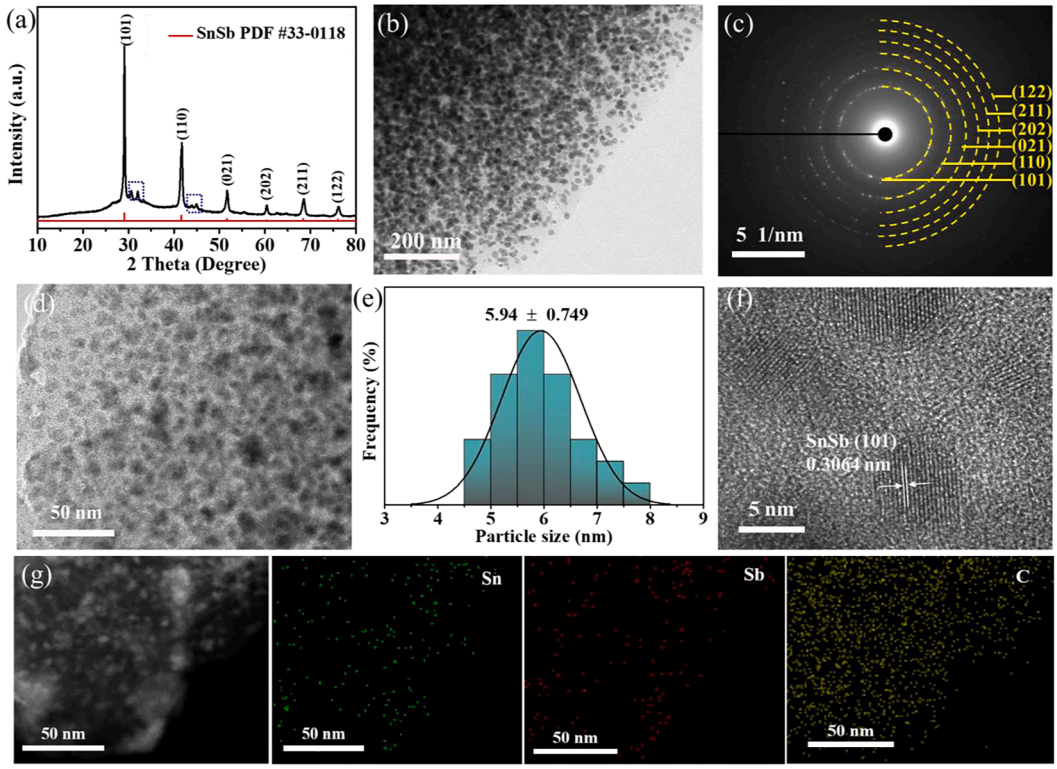

Fig. 2. (a) XRD pattern (b) TEM images, (c) SAED pattern, and (d, e) high-magnification TEM image and size distribution plot. (f) HRTEM image and (g) EDS mapping of SnSb@MAC obtained for a field of particles.

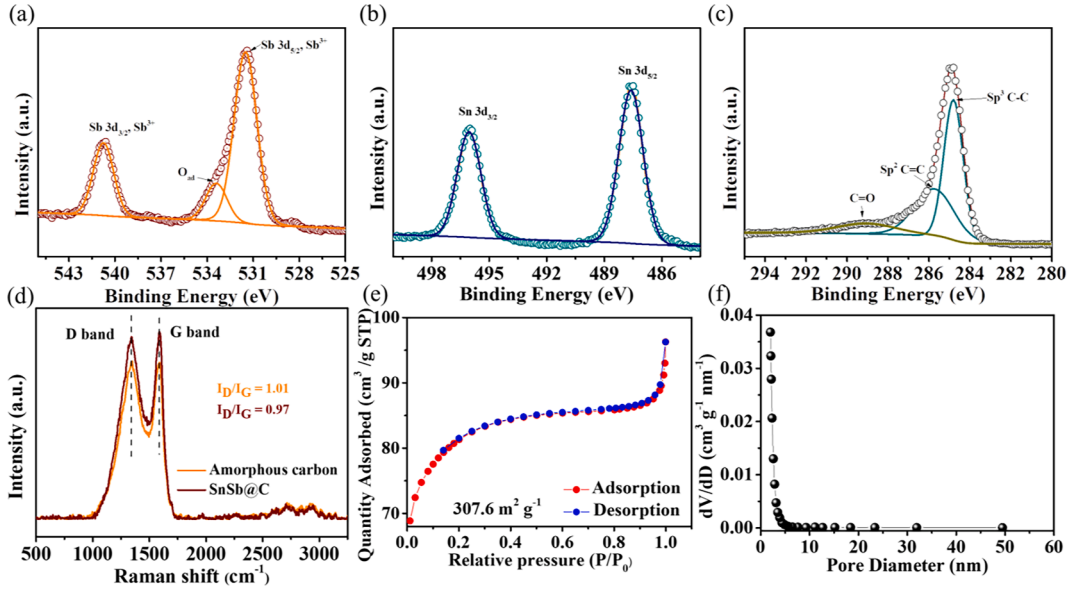

Fig. 3. High-resolution XPS spectra of (a) Sb 3d, (b) Sn 3d and (c) C1s, and (d) the Raman spectrum of SnSb@MAC and a-carbon. (e) Nitrogen adsorption–desorption isotherm and (f) pore size distribution of SnSb@MAC calculated from the adsorption isotherms using the BET method.

slightly increased. A typical nitrogen absorption/desorption isotherm is observed, indicating that its porous structure and BJH desorption pore size are 4.17 nm. The BET specific surface area of SnSb@MAC is 307.6 $m^2\ g^{-1}$ (Fig. 3**e and 3f**). However, this type of carbon shows a solid structure, but there are without obvious pores from the SEM image (Fig. S2) [38]. In addition, pore size distribution curve suggests the presence of a proportion of micropores. It can also be seen that the isothermal curve has a small hysteresis loop, revealing there are some micropores (<2 nm). The coexistence of mesopores and micropores are responsible to promote the capacitive contribution and alleviate the volume contraction/expansion during cycling process [38]. Its porosity and specific surface area can enhance the non-Faradaic contribution and reactivity of composite given a mention in the section of electrochemical analysis at high current rate.

The electrochemical performance of SnSb@MAC is evaluated in Fig. 4. According to the cyclic voltametric curve in Fig. 4a, the SEI layer is firstly formed from 1.2 V to 0.75 V (centered at 0.89 V) on the initial discharge curve. When the scan is below 0.75 V (centered at 0.5 V and

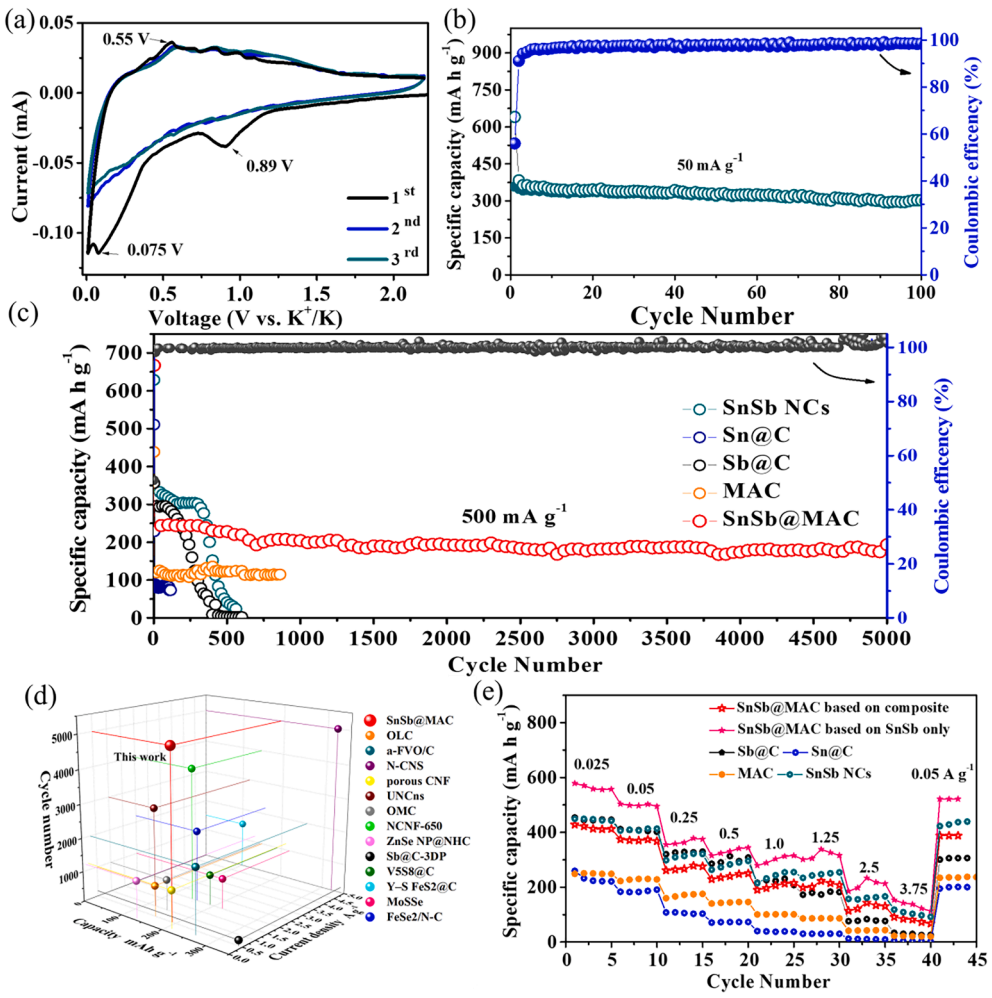

Fig. 4. Electrochemical performance of SnSb@MAC: (a) cyclic voltammetry of SnSb@MAC at sweeping rate of 0.1 mV s^{-1}. (b) the cycling performance of SnSb@MAC at current density of 50 mA g^{-1}. (c) Cycling performance of all materials in this work at the current density of 50 mA g^{-1} for first three cycles and 500 mA g^{-1} for other cycles. (d) The comparison between this work and other reported literatures. (e) The rate performance of all materials in this work at various current densities from 25 mA g^{-1} to 3750 mA g^{-1}.

0.075 V), the broad peak can be attributed to the irreversible K insertion in the carbon defects and the irreversible conversion reaction of surface oxides, which is consistent with the XPS analysis. In the subsequent cycles, the CV curves display a similar shape due to the reversible reaction. At a low charging rate of 50 mA g^{-1}, the SnSb@MAC provide a reversible capacity of approximately 312 mA h g^{-1} after 100 cycles (Fig. 4b). The initial cycle of SnSb@MAC (first discharge capacities: 677.3 mA h g^{-1} at 50 mA g^{-1}) is shown in Fig. S6, and then the current rate is increased to 500 mA g^{-1} to examine the cyclability of the SnSb@MAC. For the first 100 cycles, the cycling performances of all materials have been shown in Fig. S7, while the corresponding voltage profiles are shown in Fig. S8 and S9. SnSb@MAC exhibits an outstanding cycling stability in Fig. 4**c**, with a reversible capacity of ~200 mAh g^{-1} after 5000 cycles (the fluctuation of long-term cycling test can be attributed to temperature change of the surrounding environment). In the first cycles, the capacities of SnSb NCs and Sb@C (302.1 mAh g^{-1} and 288.0 mAh g^{-1}) is higher than that of SnSb@MAC, but the rapid capacity decay (SnSb NCs after 308 cycles) and (Sb@C after 110 cycles) indicated that the poor cyclability owing to the lack of carbon layer and larger particle size. In addition, Sn@C can provide a capacity of 245.1 mA h g^{-1} at current density of 50 mA g^{-1}, but seriously reduced to ~82.3 mAh g^{-1} as the current density is increased to 500 mA g^{-1}. The Nyquist plots of the SnSb@MAC composites at initial cycle are shown in Fig. S23. The charge-transfer resistance of SnSb@MAC decreases gradually with a changing voltage of the SnSb@MAC after discharging and charging process. The decreased resistance can enhance the ionic conductivity of the composite, which is beneficial for the insertion/extraction of K^+ ions into/from the anodes [17]. Compared to the other reported literatures (Table S1 and Fig. 4**d**) [5,6,23,39-48] and SnSb composite (Table S2), the benefits of multi-functional constituents have been shown, such as smaller size of SnSb induced by Sn and chelating agent, the ultra-stability of MAC, the synergy between Sn, Sb and MAC, and the great cycling performance. To interpret the rate capability, we evaluate the performance of electrodes at various current rates from 0.025 to 3.75 A g^{-1}. Fig. 4**e** and **Fig. S10** show that the rate performance of SnSb@MAC calculated based on composite (red star), which delivers the specific capacity of 413.4, 370.4, 278.6, 248.2, 213.25, 208.0, 143.5 and 91.3 mA h g^{-1} at the current density of 0.025, 0.05, 0.25, 0.5, 1, 1.25, 2.5 and 3.75 mA g^{-1}, respectively. The different ratio of active material is presented in supporting information (Fig. S11). The Sn@C delivers relatively poor performance, and the capacity of Sb@C is lower than that of SnSb@MAC when current density up to 1.0 A g^{-1}. With the synergetic effect of Sn and Sb, the rate performance of SnSb@MAC is better than others [13]. Concerned about the content and reactivity of MAC, we have calculated the values of capacity contribution of SnSb and carbon given in Table S3. Based on the data, the contribution of carbon gradually decreases as the current density increases. If the material is a fluffy scaffold, its rate capability and capacitive contribution at high current rate will be better than non-fluffy material [16]. This result can be attributed to the lack of fluffy structure of composite prepared by sol–gel method, but the synergetic effect of SnSb nanoparticles improves the weakness of the composite. In particular, the capacity of SnSb@MAC (pink star in Fig. 4e) can be recalculated and described in term of the content of SnSb (53 wt%) and the capacity contribution ratio (Table S3). Consequently, the rate performance of SnSb embedded in MAC is not significantly different from that of SnSb NC. According to the

electrochemical results after calibrating, the SnSb@MAC not only has the excellent cyclability, but also maintains a good rate capability compared with SnSb NCs.

In order to further explore electrochemical behaviors of SnSb@MAC electrodes, the kinetic behaviors are systematically analyzed by CV analysis. Based on CV curves of SnSb@MAC in Fig. 5**a.** The relationship between the sweeping rate (ν) and measured current (I_p) can be expressed as the equation:

$$I_p = a\nu^b$$

Normally, the b value approaches to 0.5 or 1.0 indicated an ideal Fardaic or non-Fardaic reaction domain. Here, a Fardaic reaction is involved with intercalation, alloying and conversion reaction, and then a non-Fardaic reaction is centred at adsorption and desorption. If b were an interval value between 0.5 and 1.0, illstrustating that the material is controlled simoutinously by two electrochemical behaviors; The value of b presented in Fig. 5**b** can be acquired from plotting the log(ν) versus log (I_p), and the b for cathodic and anodic peaks of SnSb@MAC are 0.8129 and 0.8839, respectively. The results of SnSb@MAC electrodes are dominated simoutinously by capacitve and diffusive behaviors. In addition, the relationship between capacitive contribution ($k_1\nu$) and the diffusive contribution ($k_2\nu^{0.5}$) as the following [11,49,50]:

$$I = k_1\nu + k_2\nu^{0.5} \quad (1)$$

$$I/\nu^{0.5} = k_1\nu^{0.5} + k_2 \quad (2)$$

After transformating Eq. (1) toward (2), k_1 and k_2 are slope and intercept, repecitvely, acquired by plotting the I / $\nu^{0.5}$ versus $\nu^{0.5}$. On basis of the result, the contribution ratio of SnSb@MAC has accounted of 71.2% at 1.0 mV s^{-1} enhanced slightly by MAC, as exhibited in Fig. 5**c**. Moreover, the contribution ratio is augmented with the increase of scan rate (Fig. 5**d**), illustrating that both diffusive and capacitive contribution in high-current region should not be reckoned with. In addition, the pseudocapacitive effect of SnSb@MAC may be attributed to the defect of the disordered carbon for extra K^+ storage, which can promote electrochemical reactions and enhance storage efficiency [51]. During low sweeping rate, the diffusion-controlled K^+ storage can take place mainly on inner region of materials, and can proceed with Faradic reaction, making it favorable for long-term reversibility and rechargeability. Moreover, the capacitive and diffusive reaction can synchronously contribute to the electrochemical performance when sweeping at 1.0 mV s^{-1}. In addition, the capacitive contribution of MAC and SnSb NCs are shown in Fig. S12 (a-d) and Fig. S13 (a-d). Although the capacitive contribution of SnSb NCs has quantified of 66.9%, which is less than that of others, the rate performance of SnSb NCs (Fig. 4e) are better than that of SnSb@MAC based on weight of composite. This condition can be resulted from the good rate retention of SnSb itself. When the current density gradually increases, the difference of capacity between SnSb@MAC and SnSb NCs decreases due to the benefit of carbon. Therefore, the amorphous carbon prepared by polyesterification method can not only give SnSb alloy a ultra-stable host but also promote the rate capability.

The galvanostatic intermittent titration technique (GITT) analysis present in Fig. 5**e, Fig. S11 and Fig. S12** and the corresponding equations are evaluated as the following:

$$D = \frac{4}{\pi\tau}\left[\frac{mV_m}{MS}\right]^2\left[\frac{\Delta E_s}{\Delta E_t}\right]^2 \approx \frac{4}{\pi\tau}[L]^2\left[\frac{\Delta E_s}{\Delta E_t}\right]^2 \quad (3)$$

Note that the average thickness of electrodes is measured by cross-section SEM image shown in Fig. S14. The diffusion coefficient of SnSb@MAC ($D_{SnSb@MAC}$) are calculated to range from 10^{-10} to 10^{-12} cm^2 s^{-1} (cencerted at 10^{-11}). The MAC and SnSb NCs are concerted at $10^{-9} \sim 10^{-10}$ and $10^{-11} \sim 10^{-12}$. Notably, the diffusion coefficients of SnSb@MAC decline gradually at the potassiation state closed to 1.0, with a voltage-dependent features since the alloying reaction of K^+ occured at this stage. Moreover, the diffusivity acquired from GITT results always assumes that it is a diffustion-dominated step for the K^+ transport in agreement with Fick's second law [49]. Therefore, GITT analysis is conducted at quite slow current rate (50 mA g^{-1}), meaning that the $D_{SnSb@MAC}$ is consisent with the CV results in which the diffusion contribution is accounted of 60% at the low sweep rate (0.1 mV s^{-1}); that is, the potassiation/de-potassiation reaction is a process dominated by diffusion-limited behavior. The trend in diffusivity of SnSb@MAC, amorphous carbon (**Fig. S12e**) and SnSb NCs (**Fig. S13e**) are consistent with the results of CV analysis.

To further explain the structural evolution upon K^+-insertion and extraction, the *in-situ* contour mapping and *ex-situ* XRD patterns are used to observe the structural evolution and reaction mechanism of

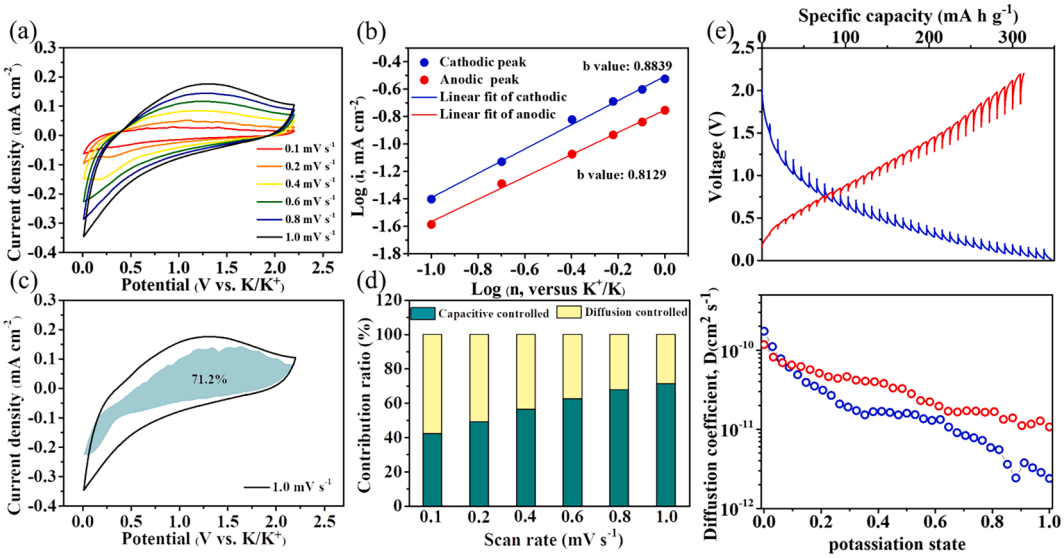

Fig. 5. Electrochemical analysis of kinetic behavior of the SnSb@MAC. (a) The cyclic voltammetry curves at various scan rate from 0.1 to 1.0 mV s^{-1}, (b) the corresponding log(i) as a function of log(ν) at the anodic and cathodic peak. (c) pseudocapacitive and diffusion-controlled condition at 1.0 mV s^{-1}, and (d) normalized contribution ratio of surface kinetic and diffusive capacities at various scan rate from 0.1 to 1.0 mV s^{-1}. (e) GITT curves and diffusion coefficient of SnSb@MAC half-cell during different potassiation (blue) and depotassiation (red) state based on current of 50 mA g^{-1} for 10 min, followed by a 1-hour relaxation. (For interpretation of the references to colour in this figure legend, the reader is referred to the web version of this article.)

SnSb@MAC. Fig. 6a displays the *in-situ* XRD and corresponding voltage profile in the left and right columns, respectively. Additionally, the *in-situ* XRD analysis of MAC is also shown in Fig. S15. The proposed mechanism and the original line plot (Fig. S16) of the operando XRD analysis of SnSb@MAC are obtained in the first three cycles. Initially, the fresh electrode has been discharged from the open-circuit potential (OCP, ~2.9 V), and the broad peak of amorphous carbon is centered at 24°, indicating that structure is disordered and overlapping with the SS-mesh signal. In the initial period of discharging process, the peaks do not shift significantly due to a large amount of K^+ adsorption. This result mainly occurred in the surface defect area of the composite material and has been no significant effect on the structural deformation of MAC. Afterward, the MAC undergoes a structural transformation, which indicates that the change in 2θ at ~23.0° at 0.01 V reaches its limit. Additionally, the intensity of diffraction peak of MAC is reduced and broadened. Therefore, the interlayer distance of MAC is expanded with increased distortedness due to K^+-insertion reaction, being similar to the previous reported literature [30]. Simultaneously, the peaks of SnSb at 29.11° and 41.64° have moved slightly toward higher angle. On the basis of Bragg's law, the 2θ will be increased with the d-spacing decreased. The ion radius of K^+ is much smaller than that of Sn (or Sb). Therefore, this can be achieved through the substitution of Sn or Sb in the Rhombohedral SnSb cell with K^+ during the potassiation process, assuming that the final voltage at 0.01 V is for K_α(Sn, Sb). In order to determine that the potassiation/depotassiation process is reversible, the *ex-situ* XRD experiment of SnSb@MAC are investigated after the first cycle (Fig. 6b) and after the 100 th cycle (Fig. 7a). Fig. 7d further indicates that the d-spacing of the two diffraction rings is changed from 0.3067 Å to 0.3025 Å and from 0.2176 Å to 0.2134 Å, respectively. Likewise, the TEM and HR-TEM images (Fig. 7b and 7c) also have similar (1 0 1) plane d spacing values in the selected area diffraction results. In the subsequent depotassiation process where the voltage is increased from 0.01 V to 2.2 V, the SnSb and MAC peak gradually recovered, indicating that K^+ may undergo reversible de-alloying and de-intercalation reactions. In addition, Fig. 7e, 7f and 7 g show that the TEM, HRTEM and ring patterns of SnSb@MAC at 2.2 V, revealing that the d-spacing returns to close to 0.3067 Å (0.3062 Å) and 0.2176 Å (0.2171 Å), which can be assigned to (1 0 1) and (1 1 0) plane, respectively. The EDS mapping before and after cycling process have been shown in Fig. S17. According to the above results, the proposed mechanism is schematically illustrated in Fig. 6c, as summarized below:

Stage I:

$$MAC + K^+ + e^- \rightarrow Adsorbed\ K^+(MAC) + SEI\ formation(OCP \sim 0.38V)$$

Stage II:

$$SnSb + MAC + K^+ + e^- \rightarrow K_\alpha(Sn, Sb)(low\ crystalline) + intercalated\ K^+(MAC)(0.38 \sim 0.01V)$$

Stage III:

$$K_\alpha(Sn, Sb) + intercalated\ K^+(MAC) - K^+ - e^- \rightarrow SnSb + MAC(2.2V)$$

At the beginning of potassiation process from 2.9 V, K ions are adsorbed on the electrode surface and and the irreversible SEI layer

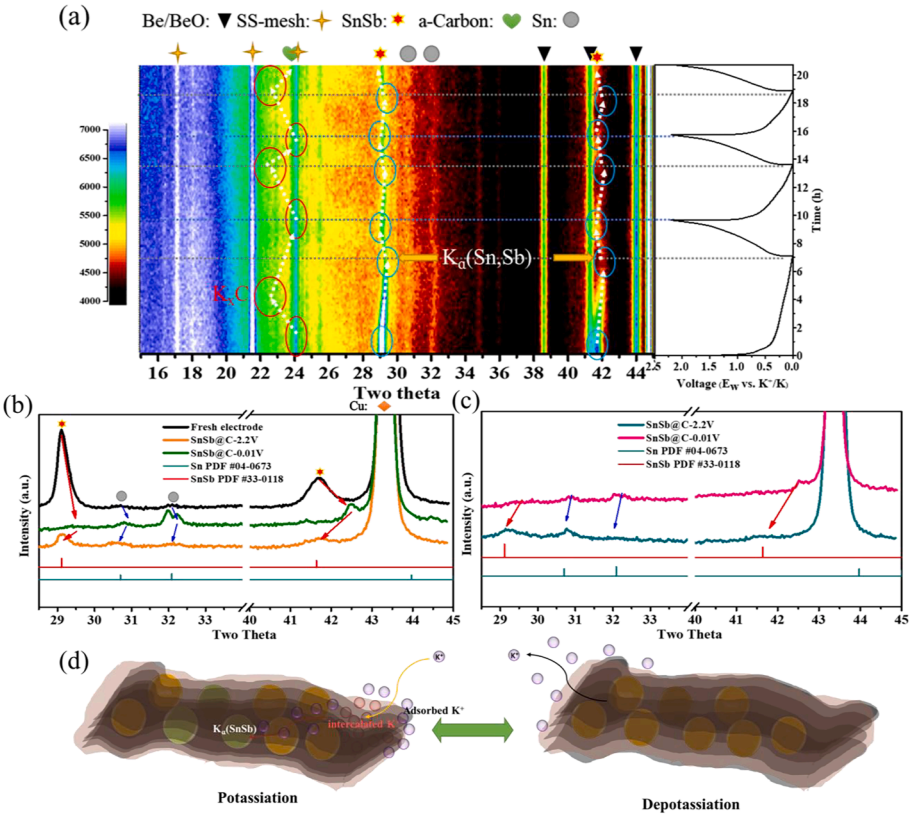

Fig. 6. (a) *in-situ* contour plot of the operando XRD pattern obtained for the initial cycles of SnSb@MAC electrode. *Ex-situ* XRD results at 0.01 V and 2.2 V for (b) initial cycle and (c) after 100 cycles. (d) Schematic showing the proposed mechanism during cycling process.

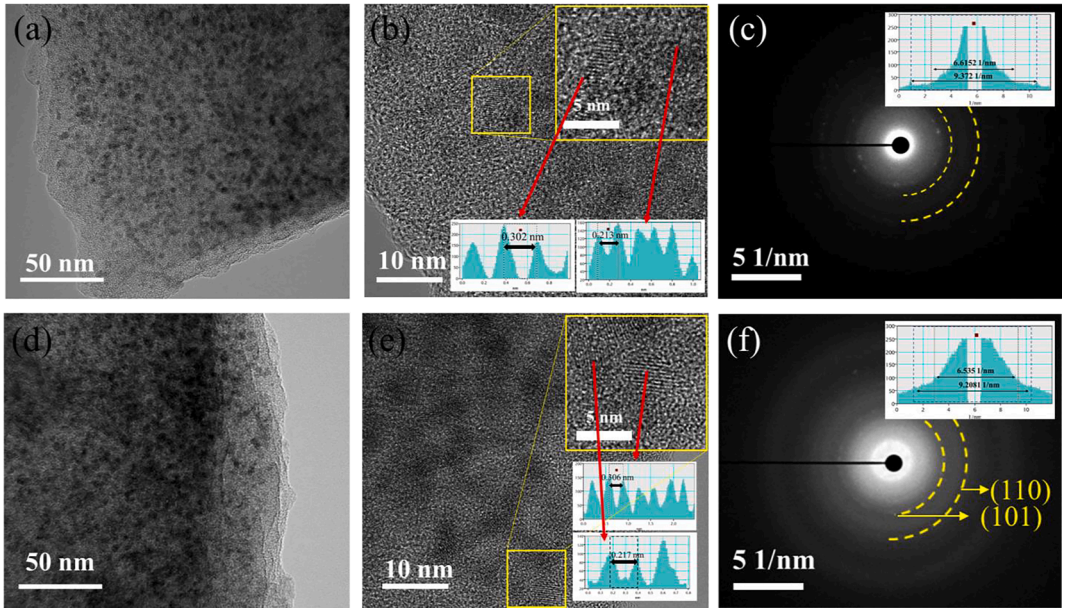

Fig. 7. TEM, HRTEM, and SAED pattern of SnSb@MAC after 100 cycles at (a-c) 0.01 V and (d-f) 2.2 V.

grows. When the discharge is lower than ~0.5 V at the stage II, the intercalation of a-carbon and formation of K_q (Sn,Sb) alloy occur. In the depotassiation region, the de-alloying reaction of SnSb was ionized and returned to the unit cell of SnSb. Furthermore, the deintercalation of a-carbon was also characterized by operando XRD. Although porous carbon can enhance the contribution of the pseudo-capacitance, the strong scaffold also limits the complete potassiation of such K_3Sb and KSn, and their phase transition and volume expansion are larger than K_q (Sn,Sb). Experimental verification shows that the capacity of SnSb NCs is 1.5 times the capacity of SnSb@MAC, but the capacity of SnSb NCs will be severely attenuated after 300 cycles. It is worth noting that the ex-situ analysis of SnSb NCs cannot be restored to the original position (Fig. S18). Therefore, due to the reduced phase transition, the structure/composition evolution mechanism confirms a highly reversible alloying reaction and excellent cyclability.

Furthermore, we demonstrate the assembly of PIB full cells SnSb@MAC anode with PTCDA cathode (Fig. 8**a**). According to the voltage profile given in Fig. 8**b**, the capacity of the PTCDA cathode at 500 mA g^{-1} is 117 mA h g^{-1} and the potential range is 1.5 to 3.5 V. The electrolyte solution used in the full cell is identical to the half cell, and the working voltage interval is 0.5 to 3.4 V. The charge curve of a SnSb@MAC// PTCDA full cell should appear within the interval, which is implied by the respective half-cell voltage curves of SnSb@MAC and PTCDA. Fig. 8**b** shows that two prominent plateaus appear in the blue curve, which are 2.0 V ~ 2.5 V (charging plateaus) and 1.65 V ~ 1.0 V (discharging plateaus). The CV curve showed a good overlapping shape

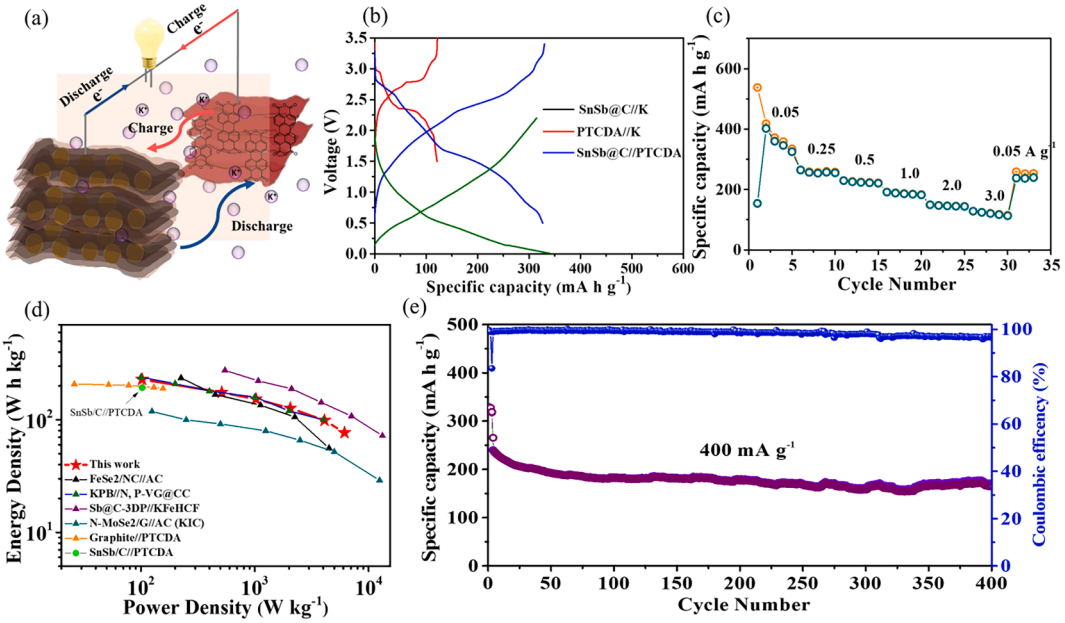

Fig. 8. PIB full cell using a SnSb@MAC anode and a PTCDA cathode. (a) Schematic (b) charge/discharge curves of PTCDA cathode, SnSb@MAC anode, and SnSb@MAC //PTCDA coin full cells; (c) rate performance (based on active material of anode) and (d) Ragone plot of SnSb@MAC and other literatures were compared based on the total mass of active materials of cathode and anode. (e) electrochemical cycling performance at 400 mA g^{-1} (based on active material of anode).

in the fifth and sixth cycles, indicating that SnSb@C// PTCDA PIB full cells are reversible (**Fig. S19**). Furthermore, corresponding to **Fig. S20**, the voltage profile of the coin full cell in the first three cycles that slowly decay from the 1 st to 3rd could be attributed to the unequal areal capacity of the anode and the cathode. The initial discharging curve is derived from the open circuit potential (OCP). Therefore, the specific capacity of the initial discharging cycle is lower than the specific capacity of other cycles. Fig. 8**c** demonstrates the rate capability of the PIB full cell and the corresponding voltage profiles (**Fig. S21**) with specific capacities were 335.0, 257.2, 223.6, 185.9, 145.2 and 113 mA h g^{-1} (based on the active mass of anode) at current densities of 0.05, 0.25, 0.5, 1.0, 2.0 and 3.0 A g^{-1}, respectively. In addition, the areal capacities between the anode and cathode were paired based on a current density of 0.5 A g^{-1}. The Ragone plot of SnSb@MAC shows the excellent performance in Fig. 8**d**: all data from the reported literature is recalculated based on total mass of active material of anode and cathode [52]. According to the Ragone plot [19,41,47,53,54], the full cell of SnSb@MAC//PTCDA delivered an energy density of 228.9 W h kg^{-1} and 77 W h kg^{-1} at a power density of 103 W kg^{-1} and 6150 W kg^{-1}, respectively. When the current density is maintained at 400 mA g^{-1} (orange and purple curves in **Fig. S20**), the overlapping shape in the cycles indicates that SnSb@MAC// PTCDA full cell has good reversibility and cyclability. The cell exhibited long-term cycle life. The initial specific charge capacity of 328 mA h g^{-1} (based on the active mass of anode) is shown in Fig. 8**e**. Under an average charge voltage of 2.05 V, a reversible discharge specific capacity at 400 mA g^{-1} is 177 mA h g^{-1} after 400 cycles. However, the specific capacity of SnSb@MAC full cell is lower than that of the half cells, perhaps due to the capacity mismatch between the positive electrode and negative electrode. However, when the full cell is performed after 300 cycles, the Coulombic efficiency of full cell decreased rapidly due to the limitation of the PTCDA cathode (**Fig. S22**). The electrochemical results of the full cell are beneficial to the synergy of the composite material, indicating that the half-cell of SnSb@MAC proves the feasibility of the SnSb@MAC anode in PIBs with high rate capability and structural durability.

10. Conclusion

In summary, the ultrasmall SnSb embedded in mesoporous amorphous carbon was synthesized via the polyesterification-assisted thermal pyrolysis/reduction strategy. The characteristic structure and electrochemical results through the introduction of Sn and amorphous carbon can effectively relieve the volume change of SnSb@MAC composite. Thanks to the synergistic effect of alloying and intercalation mechanism, the cycle performance of the composite anode has been greatly improved compared with using each single component alone. In addition, the full PIB constructed by coupling the PTCDA cathode and the composite anode has a maximum energy density of 228.9 W h kg^{-1}, a maximum power output of 6150 W kg^{-1}, and a good cycle lifespan. The structural evolution of operando XRD shows that a reversible reaction mechanism, i.e., (Sn,Sb) ⇆ K_6(Sn,Sb), in the potassiation/ depotassiation processes of SnSb@MAC composites. This study proposes a reliable way to obtain a synergistic composite material that confines ultrasmall SnSb in MAC to prevent agglomeration of nano-sized particles, thereby greatly extending cycle life and comparable to full cell applications.

Author contributions

The manuscript was written through contributions from all the authors. All the authors have given their approval for the final version of the manuscript.

Declaration of Competing Interest

The authors declare that they have no known competing financial interests or personal relationships that could have appeared to influence the work reported in this paper.

Acknowledgements

We acknowledge the financial support by the Ministry of Science and Technology through the grants of MOST-110-2628-E-007-001.

Appendix A. Supplementary data

Supplementary data to this article can be found online. Details on material and electrochemical characterization; SEM images, XRD pattern, and electrochemical performance of SnSb@MAC; GITT results and diffusion coefficient of SnSb NCs and MAC; *in-situ* XRD of MAC; cycling performance of PTCDA; CV curve, voltage profile of SnSb@MAC//PTCDA. Supplementary data to this article can be found online at https://doi.org/10.1016/j.cej.2021.130451.

References

[1] J. Zhou, Y. Liu, S. Zhang, T. Zhou, Z. Guo, InfoMat 2 (2020) 437–465.
[2] J. Ge, X. Yi, L. Fan, B. Lu, J. Energy Chem. 57 (2021) 28–33.
[3] Q. Zhang, X. Cheng, C. Wang, A.M. Rao, B. Lu, Energy Environ. Sci. 14 (2021) 965–974.
[4] M. Chen, Y. Cao, C. Ma, H. Yang, Nano Energy 81 (2021), 105640.
[5] Y. Xu, C. Zhang, M. Zhou, Q. Fu, C. Zhao, M. Wu, Y. Lei, Nat. Commun. 9 (2018) 1–11.
[6] W. Wang, J. Zhou, Z. Wang, L. Zhao, P. Li, Y. Yang, C. Yang, H. Huang, S. Guo, Adv. Energy Mater. 8 (2018) 1701648.
[7] C. Gao, Q. Wang, S. Luo, Z. Wang, Y. Zhang, Y. Liu, A. Hao, R. Guo, J. Power Sources 415 (2019) 165–171.
[8] K.-T. Chen, S. Chong, L. Yuan, Y.-C. Yang, H.-Y. Tuan, Energy Stor. Mater. 39 (2021) 239–249.
[9] Q. Wang, C. Gao, W. Zhang, S. Luo, M. Zhou, Y. Liu, R. Liu, Y. Zhang, Z. Wang, A. Hao, Electrochim. Acta 324 (2019), 134902.
[10] H. Ding, J. Zhou, A.M. Rao, B. Lu, Natl. Sci. Rev. (2020).
[11] W. Hong, Y. Zhang, L. Yang, Y. Tian, P. Ge, J. Hu, W. Wei, G. Zou, H. Hou, X. Ji, Nano Energy 65 (2019), 104038.
[12] H. Zhao, C. Zhuang, J. Xu, Z. Zhang, W. Shen, H. Tang, Y. Wang, T. Xu, X. Wang, X. Li, Ionics 26 (2020) 5019–5028.
[13] V. Gabaudan, R. Berthelot, M.T. Sougrati, P.-E. Lippens, L. Monconduit, L. Stievano, J. Mater. Chem. A 7 (2019) 15262–15270.
[14] X.-T. Zheng, K.-T. Chen, Y.-Y. Hsieh, H.-Y. Tuan, ACS Sustainable Chem. Eng. 8 (2020) 18535–18544.
[15] C.-Y. Tsai, C.-H. Chang, T.-L. Kao, K.-T. Chen, H.-Y. Tuan, Chem. Eng. J. 417 (2021), 128552.
[16] S.-B. Huang, Y.-Y. Hsieh, K.-T. Chen, H.-Y. Tuan, Chem. Eng. J. 416 (2020), 127697.
[17] K.-T. Chen, H.-Y. Tuan, ACS Nano 14 (2020) 11648–11661.
[18] H. Ding, J. Wang, L. Fan, Z. Liu, X. Jia, X. Yu, B. Lu, Chem. Eng. J. 395 (2020), 125147.
[19] J. Wu, Q. Zhang, S. Liu, J. Long, Z. Wu, W. Zhang, W.K. Pang, V. Sencadas, R. Song, W. Song, Nano Energy 77 (2020), 105118.
[20] Z. Wang, K. Dong, D. Wang, S. Luo, Y. Liu, Q. Wang, Y. Zhang, A. Hao, C. Shi, N. Zhao, J. Mater. Chem. A 7 (2019) 14309–14318.
[21] Z. Wang, C. Duan, D. Wang, K. Dong, S. Luo, Y. Liu, Q. Wang, Y. Zhang, A. Hao, J. Colloid Interface Sci. 580 (2020) 429–438.
[22] Z. Wang, K. Dong, D. Wang, F. Chen, S. Luo, Y. Liu, C. He, C. Shi, N. Zhao, Chem. Eng. J. 371 (2019) 356–365.
[23] Y. He, L. Wang, C. Dong, C. Li, X. Ding, Y. Qian, L. Xu, Energy Stor. Mater. 23 (2019) 35–45.
[24] W. Xiao, X. Li, B. Cao, G. Huang, C. Xie, J. Qin, H. Yang, J. Wang, X. Sun, Nano Energy 83 (2021), 105772.
[25] L. Xing, K. Han, Q. Liu, Z. Liu, J. Chu, L. Zhang, X. Ma, Y. Bao, P. Li, W.A. Wang, Energy Stor. Mater. 36 (2021) 309–317.
[26] S. Bao, S.-H. Luo, S.-X. Yan, Z.-Y. Wang, Q. Wang, J. Feng, Y.-L. Wang, T.-F. Yi, Electrochim. Acta 307 (2019) 293–301.
[27] C. Liu, S. Luo, H. Huang, Y. Zhai, Z. Wang, ChemSusChem 12 (2019) 873–880.
[28] M. Ickler, M. Devi, I. Rogge, J. Singh, A. Kumar, J. Mater. Sci. Mater. Electron. 31 (2020) 6977–6987.
[29] M. Walter, S. Doswald, M.V. Kovalenko, J. Mater. Chem. A 4 (2016) 7053–7059.
[30] L. Fan, R. Ma, J. Wang, H. Yang, B. Lu, Adv. Mater. 30 (2018) 1805486.
[31] J. Zheng, Y. Yang, X. Fan, G. Ji, X. Ji, H. Wang, S. Hou, M.R. Zachariah, C. Wang, Energy Environ. Sci. 12 (2019) 615–623.
[32] A.E. Danks, S.R. Hall, Z. Schnepp, Mater. Horiz. 3 (2016) 91–112.
[33] H. Okamoto, J. Phase Equilibria. Diffus. 33 (2012) 347-347.
[34] P. Xiong, J. Wu, M. Zhou, Y. Xu, ACS Nano 14 (2019) 1018–1026.
[35] K. Mahendraprabhu, P. Elumalai, J. Chem. Sci. 128 (2016) 831–837.
[36] Z. Huang, Z. Chen, S. Ding, C. Chen, M. Zhang, Solid State Ionics 324 (2018) 267–275.

[37] J. Qin, T. Wang, D. Liu, E. Liu, N. Zhao, C. Shi, F. He, L. Ma, C. He, Adv. Mater. 30 (2018) 1704670.
[38] R. Guo, X. Liu, B. Wen, F. Liu, J. Meng, P. Wu, J. Wu, Q. Li, L. Mai, Nanomicro Lett. 12 (2020) 1–12.
[39] X. Niu, Y. Zhang, L. Tan, Z. Yang, J. Yang, T. Liu, L. Zeng, Y. Zhu, L. Guo, Energy Stor. Mater. 22 (2019) 160–167.
[40] J. Chen, B. Yang, H. Li, P. Ma, J. Lang, X. Yan, J. Mater. Chem. A 7 (2019) 9247–9252.
[41] L. Fan, R. Ma, Q. Zhang, X. Jia, B. Lu, Angew. Chem. Int. Ed. Engl. 58 (2019) 10500–10505.
[42] X. Zhao, P. Xiong, J. Meng, Y. Liang, J. Wang, Y. Xu, J. Mater. Chem. A 5 (2017) 19237–19244.
[43] Y. Zhao, J. Zhu, S.J.H. Ong, Q. Yao, X. Shi, K. Hou, Z.J. Xu, L. Guan, Adv. Energy Mater. 8 (2018) 1802565.
[44] L. Li, W. Zhang, X. Wang, S. Zhang, Y. Liu, M. Li, G. Zhu, Y. Zheng, Q. Zhang, T. Zhou, ACS Nano 13 (2019) 7939–7948.
[45] J. Qin, H.M.K. Sari, C. He, X. Li, J. Mater. Chem. A 7 (2019) 3673–3681.
[46] H. Huang, R. Xu, Y. Feng, S. Zeng, Y. Jiang, H. Wang, W. Luo, Y. Yu, Adv. Mater. 32 (2020) 1904320.
[47] X.-D. He, Z.-H. Liu, J.-Y. Liao, X. Ding, Q. Hu, L.-N. Xiao, S. Wang, C.-H. Chen, J. Mater. Chem. A 7 (2019) 9629–9637.
[48] H. He, D. Huang, Q. Gan, J. Hao, S. Liu, Z. Wu, W.K. Pang, B. Johannessen, Y. Tang, J.-L. Luo, ACS Nano 13 (2019) (1852) 11843–11851.
[49] L. Qin, N. Xiao, J. Zheng, Y. Lei, D. Zhai, Y. Wu, Adv. Energy Mater. 9 (2019) 1902618.
[50] J. Feng, S.-H. Luo, S.-X. Yan, Y. Zhan, Q. Wang, Y.-H. Zhang, X. Liu, L.-J. Chang, J. Mater. Chem. A 9 (2021) 1610–1622.
[51] L. Liu, Y. Chen, Y. Xie, P. Tao, Q. Li, C. Yan, Adv. Funct. Mater. 28 (2018) 1801989.
[52] Y. Hu, W. Tang, Q. Yu, X. Wang, W. Liu, J. Hu, C. Fan, Adv. Funct. Mater. 30 (2020) 2000675.
[53] J. Ge, B. Wang, J. Wang, Q. Zhang, B. Lu, Adv. Energy Mater. 10 (2020) 1903277.
[54] Y. Yi, Z. Sun, C. Li, Z. Tian, C. Lu, Y. Shao, J. Li, J. Sun, Z. Liu, Adv. Funct. Mater. 30 (2020) 1903878.